

# 1 Early Detection of Tau Pathology

2

3 Parag Parekh<sup>1</sup>, Andrew Badachhape<sup>1</sup>, Qingshan Mu<sup>1</sup>, Rohan Bhavane<sup>2</sup>, Mayank Srivastava<sup>2</sup>, Laxman  
4 Devkota<sup>1</sup>, Jason Eriksen<sup>3</sup>, Eric Tanifum<sup>4</sup>, Ketan Ghaghada<sup>4</sup>, and Ananth Annapragada<sup>4,\*</sup>

5 <sup>1</sup>Baylor College of Medicine, Houston, TX, USA, <sup>2</sup>Texas Children's Hospital, Houston, TX, USA, <sup>3</sup> College of  
6 Pharmacy, University of Houston, Houston, TX, USA, <sup>4</sup>Texas Children's Hospital/Baylor College of  
7 Medicine, Houston, TX, USA

8 Email: annaprag@bcm.edu/avannapr@texaschildrens.org

## 9 Abstract

10 While a definitive Alzheimer's disease (AD) diagnosis remains a post-mortem exercise, the ATN  
11 Research Framework proposed by the National Institute on Aging and the Alzheimer's Association utilizes a  
12 score representing the presence of amyloid deposits (A), tau deposits (T) and neuronal degeneration markers  
13 (N), with A+T+ necessary for a positive diagnosis. Current detection of tau pathology lags amyloid detection by  
14 years and by the time both markers are detected the disease is fairly advanced. We describe the development  
15 of a new generation of molecular imaging probes for *in vivo* detection of cells undergoing abnormal  
16 phosphorylation representing the initial stages of pTau pathology, potentially enabling a very early stage  
17 diagnosis of AD. We describe a novel nanoparticle formulation that binds such abnormally phosphorylating cells  
18 in a mouse model of tau pathology, enabling *in vivo* visualization of the hyperphosphorylative state by magnetic  
19 resonance imaging. Our results demonstrate the potential of this novel platform to identify a correlative marker  
20 signifying the development of future tau pathology, and has implications for early-stage diagnosis of Alzheimer's  
21 disease.

## 22 Introduction

23 The microtubule associated protein tau, coded for by the *MAPT* gene, is abundant in the brain and is  
24 present in neurons, glia and other cell types. Tau shows immense diversity. It is expressed in six isoforms and  
25 has a vast array of post-translational modifications, including glycosylation, glycation, nitration, ubiquitination and  
26 more than 80 phosphorylation sites expanding the complexity of its role in health and disease<sup>1,2</sup>. A definitive  
27 feature of many neurodegenerative diseases including AD, frontotemporal lobar degeneration (FTLD),  
28 Parkinson's disease (PD) is the presence of intracellular aggregated filamentous tau (collectively termed  
29 "tauopathies")<sup>3-6</sup>. This pathogenic insoluble tau been implicated in disease progression in these dysfunctional

30 brains. The transition from physiological soluble tau is primarily associated with changes in its phosphorylation  
31 state leading to oligomeric tau<sup>7</sup>, then tau fibrils known as paired helical fragments (PHF) that collectively form  
32 characteristic neurofibrillary tangles (NFT). The tau aggregates are then capable of “infecting” a healthy cell  
33 inducing further misfolding, aggregation, and neuro-toxicity<sup>8,9</sup>. Studies of intercellular propagation demonstrate  
34 passage through an extracellular phase that progresses throughout the brain<sup>10,11</sup>.

35 The research framework proposed for precise diagnosis of AD by the National Institute of Aging-  
36 Alzheimer's Association (NIA-AA) categorizes extracellular deposits of amyloid beta (A), presence of  
37 intraneuronal hyperphosphorylated tau (T) and markers of neurodegeneration or neuronal injury (N). Each  
38 biomarker is scored either positive or negative<sup>12</sup>. To be on the AD continuum, A+ (Amyloid positive) is required,  
39 while a positive diagnosis of AD requires A+ and T+. Biomarker detection can be by i) positron emission  
40 tomography (PET) imaging of amyloid and tau or, ii) cerebrospinal fluid (CSF) detection of reduced Aβ<sub>42</sub>, and/or  
41 high Aβ<sub>40</sub>/ Aβ<sub>42</sub> and high phosphorylated tau and total tau, or iii) neuronal injury or degeneration as shown by  
42 structural brain magnetic resonance imaging (MRI)<sup>13</sup>. Tracking of brain pathology in longitudinal studies suggests  
43 that tau pathology may precede the accumulation of Aβ, but is undetectable as it is below current biomarker  
44 detection threshold levels, and is amplified catastrophically by independent Aβ deposition<sup>14–16</sup>. ATN research  
45 framework based diagnosis of AD is therefore limited by tau pathology detection, providing an impetus to develop  
46 specific and sensitive tau detection methods for earlier diagnosis.

47 Other factors to consider in the development of tau detection methods include the invasive nature of  
48 CSF sampling requiring lumbar puncture, and in the case of PET imaging, exposure to ionizing radiation, high  
49 cost, well documented side effects, irregular availability in primary care setting, and uneven geographical  
50 availability of PET scanners and isotopes<sup>17–21</sup>. The short half-life of PET agents also poses challenges for the  
51 detection of intracellular tau in the early stages of tau pathology formation<sup>22</sup>. Blood based markers are very  
52 promising, but only provide an indirect measure that cannot provide information on the localization of tau  
53 pathology in brain<sup>23–26</sup>. Methods to detect early tau pathology that avoid these pitfalls are therefore highly  
54 desirable.

55 The initiation of tau pathology is marked by abnormal phosphorylation of tau<sup>27,28</sup>. We hypothesize that  
56 hyperphosphorylative conditions in neurons, consistent with an altered balance of kinase-phosphatase activity  
57 resulting in elevated levels of hyperphosphorylated tau species, result in unique surface markers<sup>29–31</sup>. We  
58 envisioned a targeted contrast-enhanced MRI test identifying the earliest stages of tau pathology represented by

59 cells in the process of abnormally phosphorylating tau. We used an iterative Cell-SELEX process to identify DNA  
60 thioaptamers that specifically bound such cells<sup>32,33</sup>. The use of phosphorothioate modified aptamers enhances  
61 stability under physiological conditions. High T1 relaxivity PEGylated liposomes bearing macrocyclic Gd-  
62 chelates<sup>34</sup> were modified to bear the aptamers on their surface, thus enabling targeting of the particles to the  
63 surface of hyperphosphorylative cells for contrast-enhanced MRI. At the molecular level, we sought the binding  
64 targets of the aptamers, identifying vimentin, a normally intracellular protein that interestingly is specifically  
65 expressed on the surface of cells under hyperphosphorylative conditions, and representing a possible biomarker  
66 of pathological hyperphosphorylation found in AD.

67 **Results**

68 **Validation of cell surface changes in hyperphosphorylative conditions**

69 SH-SY5Y, a human neuroblastoma cell line that can be differentiated into neuron-like cells by changes  
70 in culture medium was used to model cell-surface changes under hyperphosphorylative conditions (Fig 1B). We  
71 used retinoic acid (RA) to induce cell differentiation marked by temporal changes in morphology including the  
72 formation and lengthening of neurites and with a strong increase in levels of intracellular tau. Imbalance in the  
73 kinase and phosphatase activity leading to hyperphosphorylation, simulating early stages of tauopathies, was  
74 induced by the use of a cell permeable neurotoxin okadaic acid (30nM, 24 h) (OA)<sup>35</sup>, and confirmed by the  
75 increase in phosphorylated tau S396 (Supp. Fig. 1). In parallel experiments, a milder agent, excitotoxin quinolinic  
76 acid (QA) 1µM for 24 h was also used to induce hyperphosphorylation<sup>36</sup>.

77 A reverse phase protein array (RPPA) assay was conducted to test the hypothesis that  
78 hyperphosphorylation results in compositional changes reflected on the cell-surface. RPPA analysis  
79 demonstrated marked cell surface changes in hyperphosphorylative cells including over-expression of cell  
80 surface receptors. RPPA assessment with a panel of 221 proteins across different pathways and post-  
81 translational modifications including phosphorylation examined SH SY5Y cell lysates under differentiated and  
82 hyperphosphorylative states. We identified 98 proteins and 36 phosphorylated proteins that showed significant  
83 change in their expression under different conditions (**Fig 1C**). Uniprot<sup>37</sup> protein associations showed 44 cell-  
84 membrane associated proteins, 10 peripheral membrane or 12 single-pass membrane proteins were significantly  
85 altered under hyperphosphorylative conditions.

86 **Screening for aptamers that bind cells in hyperphosphorylative state**

87 Aptamer screening was performed using the cell-SELEX approach on differentiated SH-SY5Y cells in a  
88 hyperphosphorylative state (Fig. 2A). A total of 26 cell SELEX cycles were performed. To remove  
89 oligonucleotides that bound common cell surface molecules not specific to the hyperphosphorylative state, a  
90 negative selection was introduced at cycles 12 and 13 using differentiated, non hyperphosphorylative cells (i.e.  
91 without OA treatment). Anticipating that selected aptamers would be systemically delivered as nanoparticle  
92 imaging agents, and the primary toxicity driven by anomalous hepatocyte uptake, we conducted another round  
93 of negative selection at cycles 20 and 21 using a hepatocyte cell-line THLE-3 to remove oligonucleotides that  
94 exhibited enhanced uptake by hepatocytes.

95 **Tau1 and Tau3 aptamers specifically bind hyperphosphorylative cells**

96 Sequencing of all the selected pools was performed using the Ion Torrent sequencing platform<sup>38</sup> and  
97 revealed the evolution of families of DNA sequences, with enrichment particularly evident after 10 rounds of  
98 SELEX. Negative selection eliminated certain sequences that were not specific to the hyperphosphorylative state,  
99 or promoting hepatocyte uptake. However, the relative abundance of key sequences increased steadily  
100 throughout the whole process. The 23 most abundant sequences at round 26 were identified and their abundance  
101 throughout the SELEX process as calculated using AptaAligner<sup>39</sup> is shown in Fig. 2B . The sequence Tau1  
102 exemplifies this behavior representing a whole 59% of cycle 26. A single base difference from this sequence,  
103 Tau3, is the second most represented sequence. The sequences present at the final round were grouped by  
104 hierarchical clustering and sequence homology using the multiple sequence alignment code MAFFT<sup>40</sup> showing  
105 five distinct families (Fig 2E) also presented as a cladogram (using the Clustal Omega<sup>41</sup>) showing the common  
106 ancestry between these five aptamers families (Fig. 2F). Elevated levels of Tau1 binding to the membrane of  
107 hyperphosphorylative cells is demonstrated in Figure 2C. The secondary structure of the aptamers Tau1 and  
108 Tau3 calculated using mfold<sup>42</sup> is shown in Fig 2D. The apparent equilibrium dissociation constants ( $K_{d_{app}}$ ) were  
109 measured by serial dilution of aptamer solutions with target hyperphosphorylated and non-target differentiated  
110 and undifferentiated SH-SY5Y cells. The affinity of these aptamers was also tested with another immortal neural  
111 progenitor stem cell line ReN-VM<sup>43</sup> in hyperphosphorylative and non-hyperphosphorylative conditions . The  $K_{d_{app}}$   
112 for Tau1 and Tau3 with hyperphosphorylated SH SY5Y cells is  $0.167 \pm 0.015$  nM and  $0.194 \pm 0.032$  nM; and  
113 for the ReN-VM cells  $318.15 \pm 46.2$  nM and  $234.24 \pm 38.6$  nM respectively (Supp. Fig 2).

114 **TauX nanoparticles for magnetic resonance imaging**

115 For *in vivo* imaging of the hyperphosphorylative state in the brain of live mice, aptamer-targeted  
116 nanoparticles were fabricated for use as a molecular MRI contrast agent (TauX). TauX, was formulated as two  
117 versions, one using the Tau1 aptamer (TauT1) and another using the Tau3 aptamer (TauT3). Liposomal  
118 nanoparticles were synthesized using a lipid mixture that included lipidized Gd-DOTA for MR imaging, cholesterol  
119 for liposomal stability; additionally we also incorporated lipidized rhodamine for studying *ex-vivo* microscopic  
120 distribution of liposomal nanoparticles in brain tissues using fluorescence microscopy<sup>44,45</sup>. The TauX  
121 compositions also included DSPE-mPEG2000 to increase the *in vivo* circulation time<sup>34</sup>. Particles had a  
122 hydrodynamic diameter of ~150nm, ~86,000 Gd-chelates per liposomes and ~500 aptamers conjugated to the  
123 outer leaflet of each liposomal nanoparticle (Fig.3)

124 ***In vivo* molecular MRI using TauX for detection of hyperphosphorylative cells**

125 To test if TauX could detect the hyperphosphorylative state *in vivo*, MRI studies were performed in a  
126 P301S transgenic mouse model of AD-related tauopathy. Studies were performed in transgenic and age-  
127 matched wild type mice at 2-3 months of age. At this young age, transgenic animals do not show frank tau  
128 pathology (i.e., neurofibrillary tangles), but practically all will develop tau pathology by around 8 months of age.  
129 Animals underwent baseline, pre-contrast MRI. Thereafter, animals were intravenously administered MRI  
130 contrast agent (TauT1, TauT3 or non-targeted control stealth liposomes that were not expected to provide signal  
131 enhancement as they did not have a targeting aptamer). Delayed post-contrast MRI was performed 4 days later.  
132 MR images were acquired using a T1-weighted spin-echo (T1w-SE) sequence and a T1-weighted fast spin echo  
133 inversion recovery (FSE-IR) sequence<sup>46</sup>. Transgenic mice administered TauT1 and TauT3 demonstrated signal  
134 enhancement in the cortex and the hippocampus regions of the brain (**Fig. 4B**). Wild-type mice (WT) administered  
135 TauT1 or TauT3 did not show signal enhancement in the brain. Similarly, transgenic mice administered non-  
136 targeted liposomal-Gd contrast agent did not show signal enhancement in cortex or hippocampus. These regions  
137 of interest were further analyzed quantitatively and signal-enhancement between the transgenic and wild-type  
138 mice were found to be statistically significant ( $p < 0.05$ ) (Fig 4D). A baseline enhancement threshold of ~6% (=2X  
139 standard deviation of signal in baseline scans) was used as the classification threshold. Animals that showed  
140 signal enhancement above the threshold were identified as positives. Receiver operator characteristic (ROC)  
141 curves were generated with a six-point ordinal scale to assess sensitivity and specificity for detecting the

142 genotype, using TauT1 and TauT3 contrast agents, and constructed over the entire tested group, including  
143 controls. The aptamer-targeted nanoparticle contrast agents, TauT1 and TauT3, showed overall AUC and  
144 accuracy of ~0.95. TauT3 demonstrated higher sensitivity than TauT1.

145 Post-mortem brain analysis was performed in 2-3 month old transgenic and wild-type mice.  
146 Immunofluorescence analysis using AT8 antibody staining revealed the presence of hyperphosphorylated tau  
147 species in transgenic mice but absent in wild type mice (**Fig. 4F**). A 100% concordance was observed between  
148 AT8 positivity and animal genotype. In summary, *in vivo* studies demonstrated that TauX enabled *in vivo*  
149 molecular MRI of the hyperphosphorylative state months before frank tau pathology i.e. the presence of  
150 neurofibrillary tangles, becomes evident in transgenic mice.

## 151 **Target identification of aptamers**

152 To characterize the binding target of the aptamers, we performed an aptamer-based pulldown assay,  
153 aptamer-based immunoprecipitation, followed by mass-spectrometry. We performed the assay for both Tau1 and  
154 Tau3, aptamers. A ranking of the abundance scores for identified proteins revealed keratin 6a, Keratin 6b and  
155 Vimentin as possible binding targets (Table 1). The surface expression of Keratin 6a, 6b was similar on wild-type  
156 and transgenic tissue sections whereas the Vim expression was higher in the transgenic mice (Fig 5C). SH-  
157 SY5Y cells under undifferentiated, and differentiated hyperphosphorylative conditions show increasing levels of  
158 vimentin (Fig.5B) further suggesting it is a potential target of aptamers Tau1 and Tau3.

## 159 **Discussion**

160 The ATN research framework suggests biomarkers to diagnose and classify AD. Under this framework  
161 CSF based detection of A $\beta$ , tau (total, and phosphorylated) have been reported but only at the prodromal stage  
162 of disease, in patients with mild cognitive impairment<sup>47</sup>. Non-invasive neuroimaging tools, such as structural MRI  
163 to diagnose and monitor neurodegeneration<sup>48</sup> show a definitive correlation with cognitive decline, visualizing  
164 atrophic regions that depict neuronal injury in late stage disease<sup>49</sup>. However, a reliable marker of early  
165 presymptomatic stage disease is yet to be identified.

166 While the role of A $\beta$  and tau in the development of AD and the mechanism of transition from  
167 presymptomatic to symptomatic AD are yet unclear, the time scale of the transition is generally accepted to be  
168 over a period of 10-20 years<sup>14</sup>. A $\beta$  deposits are considered the start of neurodegeneration but recent studies

169 indicate that tau pathology<sup>50</sup> shows a stronger correlation with disease progression suggesting that the limitation  
170 of current tests is their inability to identify early stage pathological tau<sup>15</sup>. CSF presence of hyperphosphorylated  
171 tau species p-181 and p-217 is associated with Aβ deposition that precedes a positive tau PET<sup>51</sup> but only has a  
172 concordance of 50%-70%<sup>52</sup>. Taken as a whole, the roles of Aβ and tau deposition in disease progression and  
173 the role of Aβ in the spread of initial tau aggregates, strongly suggest that a biomarker of pathological tau at a  
174 presymptomatic stage of the disease is likely to advance detection by several years, and constitutes the  
175 motivation for this work.

176 Initial tau aggregation is thought to be triggered by an imbalance in cellular homeostasis caused by  
177 dysregulated phosphorylation<sup>53,54</sup>. Several kinases can phosphorylate tau at multiple locations; at least 45 sites  
178 have been observed experimentally<sup>55-57</sup>. Combined with reduced phosphatase activities in AD, the altered  
179 kinase-phosphatase balance yields hyperphosphorylative conditions that cause abnormal hyperphosphorylation  
180 of tau<sup>58</sup>. Disruption of the normal function of tau, modulating microtubule dynamics by lowering its binding  
181 capabilities<sup>59</sup> increases the level of cytosolic free tau leading to aggregation and fibrillization of tau that spreads  
182 throughout the connected brain, seeding the pathology<sup>60,61</sup>. We hypothesized that this initial process of  
183 hyperphosphorylation is associated with changes on the surface of hyperphosphorylative cells. We therefore  
184 sought to identify these surrogate markers of tau hyperphosphorylation that presage future tau pathology.

185 Using SH-SY5Y cells as a model of neuronal hyperphosphorylation, we used a reverse-phase protein  
186 array (RPPA) analysis to demonstrate elevated levels of surface molecules specific to the hyperphosphorylative  
187 state (Fig 1C). Cell-SELEX capturing the differences between the surface of hyperphosphorylative cells and  
188 normal cells allowed the selection of phosphorothioate modified short DNA aptamers that bound with high affinity  
189 and specificity to hyperphosphorylative cells Fig 2 A. Having identified unique aptamers that bound such markers,  
190 we developed MR molecular imaging contrast agents that recognize the surface of cells in hyperphosphorylative  
191 state. We acknowledge that SH-SY5Y cells are not true neurons, they are a cell line originating in a  
192 neuroblastoma, a tumor of embryological neural crest origin. However, they can be induced to differentiate to a  
193 neuronal phenotype (as in the current work). While primary neuronal culture, or immortalized neuronal cells e.g.  
194 ReN-VM may offer alternative models of neurons, we have functionally tested the aptamer hits from our SELEX  
195 screen in a transgenic mouse model of tau deposition, and validated their performance, supporting our position  
196 that the choice of cell model was adequate to identify suitable markers of tau hyperphosphorylation.

197 PET is the leading modality for clinical molecular imaging, driven by its high contrast sensitivity, however,  
198 it suffers from poor spatial resolution on the order of 5-10mm, high cost; limited access to radioactive tracers,  
199 and radiation exposure. Nanoparticle-enhanced MR imaging overcomes all these obstacles, but historically has  
200 not achieved high enough sensitivity. We have previously demonstrated liposomal nanoparticles exhibiting large  
201 numbers of Gd chelates in the external bilayer leaflet, with hyper-T1 relaxive properties resulting in contrast  
202 sensitivity that rival nuclear imaging<sup>45,62</sup>.

203 In P301S mice, the earliest reported histopathological studies are at age of 2.5months<sup>63,64</sup>, and report  
204 no tau pathology. “Tau seeding” the cell-cell transfer of pathogenic tau aggregates has been reported using brain  
205 homogenates at 1.5 month of age<sup>65</sup>. We therefore chose P301S mice at 2 months of age for our studies when,  
206 tau seeding should be taking place, but frank tau pathology should be absent. The mice were injected with TauX  
207 nanoparticles targeted either by the Tau1 aptamer or the Tau3 aptamer. When imaged by T1-weighted MRI  
208 sequences, designed to optimize signal from the Gd chelate induced T1 relaxation caused by the liposomal-Gd  
209 nanoparticles, signal enhancement was observed in the cortex and hippocampus regions of the brain.  
210 Hyperphosphorylative conditions were confirmed by post-mortem IF staining with AT8 antibody that recognizes  
211 the S202 and T305 pTau species. Signal enhancement was not observed in non-transgenic mice, or in transgenic  
212 mice injected with untargeted nanoparticles, supporting the specificity of Tau1-or Tau3-bearing nanoparticle  
213 binding to target.

214 We have narrowed down the possible binding targets of the aptamers, and our data suggest that cell  
215 surface vimentin is a likely target. We have confirmed the specific presence of cell surface vimentin on the surface  
216 of SH-SY5Y cells in a hyperphosphorylative state, and on P301S mouse brain sections. Vimentin is an  
217 intermediate filament protein that undergoes constant assembly and/or remodeling and is usually associated with  
218 mesenchymal cells<sup>66</sup>. The assembly state of filaments is linked to their phosphorylation state, phosphorylation  
219 promotes disassembly<sup>67</sup>. Vimentin contains more than 35 phosphorylation sites targeted by multiple kinases and  
220 phosphatases allowing it to adjust IF dynamics dependent on its environment<sup>68,69</sup>. Mechanical, chemical (toxins,  
221 hypoxia), and microbial stresses upregulate vimentin and its phosphorylation that allows cells to adjust their  
222 mechanical properties<sup>70,71</sup>. The balance of different oligomeric forms influence dynamic cell processes including  
223 adhesion, migration, invasion including stress-induced signaling<sup>72</sup>. Vim IF's (~10nm) distributed throughout the  
224 cell by association with microtubules (tubulin, 24nm) regulating cell-migration, and microfilaments(actin, 7nm)  
225 regulating cell-contractility, form the cytoskeletal network and provide mechanical support for the plasma

226 membrane where it contacts other cells or the extracellular matrix<sup>73</sup>. Interestingly, during the biological process  
227 epithelial to mesenchymal transition wherein non-motile, polar epithelial cells transform to motile invasive non-  
228 polar mesenchymal cells<sup>74</sup>, cells also undergo a cytoskeletal reorganization that includes changes in cell-  
229 membrane integrity, disassembly of junction proteins, increased stress-fiber formations, altered cell-surface  
230 protein expression. Changes in the localization of proteins is a hallmark of this pathologic process. Our  
231 observation that Vimentin is upregulated and translocated to the cell surface<sup>75</sup> in the early stages of tau  
232 hyperphosphorylation suggests a possible role for EMT-related processes at the start of a slow progression  
233 towards AD pathology.

234 While positron emission tomography (PET) is the mainstay of molecular imaging, and exhibits  
235 remarkable sensitivity, there are several limitations posed by this methodology<sup>62,76</sup>. Access to PET imaging is  
236 limited, even in the relatively well-served US, and is skewed towards high density urban centers. PET costs are  
237 very high due to the need for same-day radiosynthesis, and rapid decay of the isotopes. Longer half-life isotopes  
238 cause higher radiation exposure. This tradeoff between half-life and radiation exposure greatly limit the reach of  
239 PET to a wider patient population. Current PET tau tracers recognize the tau β-sheets in the PHF and NFT  
240 present in tauopathies<sup>22</sup>. This conformation is not unique to tau and the *in vivo* specificity is circumspect limiting  
241 its interpretation. Off-target binding of Flortaucipir, an approved tau PET agent, has been reported since it binds  
242 the MAO-B enzyme in the brain<sup>77,78</sup>. Further, the vast majority of pathological tau is actually intracellular, posing  
243 a significant barrier to PET tracers that must navigate to the site of tau pathology, bind the target, and have all  
244 unbound tracer molecules cleared from the brain before the radioactive signal decays. Our choice of MRI as the  
245 detection modality is based on hyper-T1 relaxive properties of nanoparticles with surface conjugated Gd chelates,  
246 bringing detection sensitivity to the same range as nuclear imaging, and the MRI agent does not suffer from the  
247 rapid signal decay of PET agents, allowing plenty of time for unbound tracer to clear from the brain before  
248 imaging. Our choice of a cell surface surrogate marker of tau hyperphosphorylation avoids the need to bind an  
249 intracellular target. Finally, MRI imaging is already included in AD management and can be adjusted with agents  
250 such as TauX nanoparticles to constitute a highly sensitive and specific test for future tau pathology.

251 In summary, our work shows that the hyperphosphorylative conditions coinciding with the initiation of a  
252 decades long process culminating in AD result in markers manifested on the cell surface. By imaging their  
253 presence, our approach detects the presence of hyperphosphorylative cells indicative of a presymptomatic stage

254 of AD. Coupled with early amyloid detection, this test could enable early positive diagnosis using the NIA-AA  
255 research framework.

256 **Materials and Methods**

257 **Cell-lines** - SH-SY5Y cells (ATCC, Manassas, VA, #CRL-2266™) were obtained from Dr. Jason Shohet's lab at  
258 the Texas Children's Hospital, Houston, immortalized human hepatocytes (THLE-3) were purchased from  
259 American Type Culture Collection (ATCC, Manassas, VA, # CRL-11233™); both were cultured according to the  
260 ATCC instructions. ReN cell™ VM (#SCC008) cultured as per instruction using neural stem cell maintenance  
261 medium (#SCM005) and growth factors EGF (GF001) and bFGF(#GF005) all from Millipore Sigma, Burlington,  
262 MA.

263 **Differentiation** - SH-SY5Y cells were exposed to 30 µM *all-trans*-Retionic acid (Sigma-Aldrich, St.Louis, MO, #  
264 R2625) in serum free cell medium for 10 days with medium change every alternate day. ReNcell VM were  
265 differentiated by the removal of growth factors from its culture medium for 10 days.

266 **Hyperphosphorylation** - was induced in SH-SY5Y cells by addition of 30 nM okadaic acid (Sigma Aldrich,  
267 St.Louis, MO, # 459620) in growth medium with 30 µM RA for 24 hours. ReNcell VM were hyperphosphorylated  
268 using 100nM Quinolinic Acid (SigmaAldrich, St.Louis, MO, #P63204) in culture media for 24h.

269 **Synthesis of primers and TA DNA library** - All primers and Cy5, and amine labelled selected aptamers were  
270 purchased from Integrated DNA Technologies (IDT, Coralville, IA). The ssDNA library used in Cell-SELEX  
271 contained a central randomized sequence of 30 nucleotides flanked by PCR primer regions to enable the PCR  
272 amplification of the sequence (5'-CGCTCGATAGATCGAGCTTCG-(N)<sub>30</sub>-GTCGATCACGCTCTAGAGCACTG-  
273 3'). The chemically synthesized DNA library was converted to a phosphorothioate modified library by PCR  
274 amplification using, dATP ( $\alpha$ S), resulting in the DNA sequences where the 3' phosphate of each residue is  
275 substituted with monothiophosphate groups, as described previously in detail <sup>32,79</sup>. The reverse primer was  
276 labeled with biotin to separate the sense strand from the antisense strand by streptavidin-coated sepharose  
277 beads (PureBiotech, Middlesex, NJ, # MSTR0510) for the next selection round. The concentration of the TA  
278 library was determined with a NanoDrop™ 2000 by measuring the UV absorbance at 260 nm.

279 **Cell-SELEX** - The procedures of Cell-SELEX were performed according to protocol previously with some  
280 modification <sup>33,80</sup>.The initial ssDNA library of 150 pmole was dissolved in binding buffer with a total volume of 350

281  $\mu$ l. It was denatured by heating at 95°C for 5 min, then renatured by rapid cooling on ice for 10 min. The treated  
282 SH-SY5Y cells at approximately 90% confluence in a 100-mm culture plate were washed twice with washing  
283 buffer and followed by incubating with the ssDNA library of 150 pmole for 2 hrs at 4°C. Following the incubation,  
284 for positive selections, the supernatant was discarded, and cells were washed three times with washing buffer to  
285 remove any unbound sequences. Then cells were scraped off and transferred to nuclease-free water, following  
286 another three times nuclease-free water washes. Cells in nuclease-free water was centrifuged at 300 $\times$ g for 5  
287 min. QIAamp DNA Mini and Blood Mini kit (Qiagen, Germantown, MD, # 51104) was introduced to elute cell  
288 membrane fraction. The cell membrane fraction was PCR-amplified to monitor the presence of cell binding  
289 efficacy at each cycle. For negative selections, the supernatant was simply pipetted out of the flask and  
290 processed for the next cycle of selection. The desired compartment were amplified by PCR, and used to prepare  
291 the TA for the next round of selection. Two different negative selections were involved. One was differentiated  
292 treatment only SH-SY5Y cells at cycles #12 and #13. Another was hepatocyte THLE-3 cells at cycles #20 and  
293 #21. A total of 26 cycles of Cell-SELEX were conducted, including two different types of negative selections  
294 mentioned above.

295 **Next-Generation Sequencing (NGS)** - At the studied cycles, the membrane fractions were isolated and the  
296 recovered TA sequences were amplified by PCR. Equimolar quantities of the recovered TA sequences over the  
297 range were pooled together and sequenced by Next-Gen DNA sequencing using Ion318 chip (ThermoFisher,  
298 Waltham, MA). A four base sequence was introduced during PCR amplification to serve as unique “barcode” to  
299 distinguish between the studied cycles. Sequencing results were analyzed by the Aptalinger<sup>39</sup> that uses the  
300 markov model probability theory to find the optimal alignment of the sequences.

301 **Aptamer binding studies** – were conducted with undifferentiated, differentiated and hyperphosphorylated SH  
302 SY5Y and ReN cell VM grown in 96-wells seeded at 10000 per well. The apparent dissociation constants (Kds)  
303 were measured by the equation  $Y=B_{max} X / (K_d + X)$ , with GraphPad Prism 9, San Diego, CA, with a saturation  
304 binding experiment; cells were incubated with varying concentrations of Cy5-labeled aptamer in a 100  $\mu$ l volume  
305 of binding buffer containing cells, incubated for 30minutes, washed twice and resuspended in 100  $\mu$ l buffer and  
306 analyzed by Molecular probes microplate reader equipped with the appropriate excitation and emission filters.  
307 All data points were collected in triplicate.

308 **Immunocytochemistry** - Eight-well glass plate was coated with a solution of 100  $\mu$ g/ml Collagen Type I  
309 (Thermofisher Scientific, Waltham, MA, # A1064401) dissolved in 0.01N HCl and air dried, then PBS washed

310 and air dried prior to seeding 20,000 SH-SY5Y cells per well. Aptamer staining at 100 nM was performed with  
311 live cells for 2h at 4°C in binding buffer and washed twice with washing buffer. Cells were then fixed by incubation  
312 for 15 min in 4% formaldehyde in PBS at room temperature. Non-specific binding was blocked with blocking  
313 buffer (G-Biosciences, St. Louis, MO, # 786195) for 1 hour and overnight incubation at 4°C with the rabbit pTau  
314 primary antibody (1:100) (Santa Cruz Biotechnology, #: sc-101815) was followed by washing with PBS, and 1h  
315 incubation with goat anti-rabbit IgG secondary antibody, Alexa Fluor 488 (Invitrogen, Carlsbad, CA, # A-11008)  
316 for 1 hour at room temperature. Cytoskeletal actin filaments were stained with Alexa Fluor 594 Phalloidin  
317 (Invitrogen, # A12381). The cells were covered with VECTASHIELD hardset mounting medium with DAPI (Vector  
318 Laboratories, Burlingame, CA, # H-1500) for 5 min at room temperature. Images were visualized under Olympus  
319 Fluoview FV1000 confocal microscopy.

320 **TauX nanoparticle synthesis –** L- $\alpha$ -phosphatidylcholine, hydrogenated (Hydro Soy PC; HSPC) and Cholesterol  
321 were purchased from Lipoid Inc., Newark NJ, USA. 1,2-distearoyl-sn-glycero-3-phosphoethanolamine-N-  
322 [methoxy(polyethylene glycol)-2000] (DSPE-mPEG2000) was purchased from Corden Pharma, Liestahl,  
323 Switzerland. DSPE-PEG3400-COOH and Gd-DOTA-DSPE were synthesized *in house*, lis-rhodamine-DHPE  
324 from ThermoFisher Scientific. HSPC, Cholesterol, DSPE-PEG3400-COOH, DSPE-mPEG2000, Gd-DOTA-  
325 DSPE, lis-rhodamine-DHPE at molar proportions 31.4:40:0.5:3:25:0.1 were dissolved in ethanol to achieve a  
326 total concentration of 100 mM. For the non-targeted control stealth liposomes, carboxy terminated PEG was not  
327 included in the lipid mixture. The ethanolic solution of lipids was hydrated with 150mM saline solution at 65 °C  
328 for 30 minutes, allowing multilamellar liposomes to form. The mixture was then extruded in a 10ml Lipex extruder  
329 (Northern Lipids Inc., Burnaby, Canada) using a 400 nm polycarbonate track-etch polycarbonate filter (3 passes)  
330 followed by a 200 nm (3 passes) and finally 100nM filters. The suspension was then diafiltered using a MicroKros  
331 cross-flow diafiltration cartridge (500 kDa cutoff) from Repligen, Rancho Dominguez, CA, exchanging the external  
332 buffer for phosphate buffered saline (PBS, pH 7.2) for 15 volume exchanges. To form the aptamer conjugated  
333 liposomes, liposomes with lipid-PEG-COOH were reacted with amine terminated aptamers using carbodiimide  
334 chemistry. The carboxyl groups on the liposomes were activated with 5 mM EDC and 10 mM sulfo-NHS at pH~6  
335 for 5-10 minutes. The activated liposomes were then immediately reacted with the amine terminated aptamers  
336 and the pH was raised to ~7.3 - 7.6 by titrating  $\mu$ l amounts of 5 N NaOH. The final concentration of aptamers  
337 used in reaction is ~140  $\mu$ M. The reaction was mixed at room temperature for 1 hr following which the reaction  
338 was carried out at 4 deg °C overnight. The liposomes were then dialyzed against PBS to remove unconjugated

339 aptamers using a 300 kDa dialysis membrane. The dialysate (external phase) was concentrated using 10 kD  
340 centrifugal separator and washed with PBS to remove residual EDC/s-NHS. The concentrated dialysate was  
341 analysed by NanoDrop Spectrophotometer (ThermoFisher Sci., Waltham, MA, USA) to determine unconjugated  
342 aptamer fraction, and estimate aptamer density per nanoparticle in TauX formulations. Inductively coupled  
343 plasma atomic emission spectroscopy (ICP-AES) was used to measure Gd and phosphorus concentrations of  
344 TauX formulations. The hydrodynamic diameter of liposomal nanoparticles in TauX formulations was determined  
345 using a dynamic light scattering instrument.

346 **Mice** – All the procedures were performed with approval from Institutional Animal Care and Use Committee  
347 (IACUC) of Baylor College of Medicine. Mice were kept under a 12 h light/dark cycle, with food and water available  
348 ad libitum. PS19 mice from Jackson Laboratories (Bar Harbor, ME) B6; C3-Tg (Prnp-MAPT\*P301S) PS19Vle/J  
349 Stock No: 008169 were used and experiments were conducted at the 2m of age. The transgenic (TG) mice  
350 develop neurofibrillary tangles by 5 months of age<sup>64</sup>. Age-matched non-transgenic wild type (WT) mice were  
351 used as controls.

352 **Magnetic Resonance Imaging (MRI)** - MRI was performed on a 1T permanent magnet scanner (M7, Aspect  
353 Imaging, Shoham, Israel). Mice underwent pre-contrast baseline scans. Thereafter, mice were intravenously  
354 administered one of three nanoparticle MR contrast agents (TauT1, TauT3 or non-targeted control liposomes)  
355 via tail vein at a dose of 0.20 mmol Gd/kg of body weight. Delayed post-contrast MRI was performed 4 days after  
356 contrast agent injections. Pre-contrast and delayed post-contrast MR images were acquired using a T1-weighted  
357 spin echo (T1w-SE) sequence and a fast spin echo inversion recovery (FSE-IR) sequence with the following  
358 parameters: SE parameters: TR = 600 ms, TE = 11.5 ms, slice thickness = 1.2 mm, matrix = 192 × 192, FOV = 30  
359 mm, slices = 16, NEX = 4; FSE-IR parameters: TR = 13500 ms, TE = 80 ms, TI = 2000 ms, slice thickness = 2.4  
360 mm, matrix = 192 × 192, FOV = 30 mm, slices = 6, NEX = 6. Coil calibration, RF calibration, and shimming were  
361 performed at the beginning of study for each subject. The pre-contrast scans provide a baseline for calculation  
362 of signal enhancement from resulting post-contrast scans<sup>46</sup>. Two-standard deviations above the mean variation  
363 within WT control animals was used as the cutoff signal intensity for identifying tau positive animals. Six  
364 transgenic (TG) mice and six wild type mice (WT) were used for testing of each nanoparticle contrast agent  
365 formulation. Receiver operating characteristic (ROC) curves were generated on a six point ordinal scale by  
366 plotting the true positive fraction (TPF) against the false positive fraction (FPF) based on imaging-based  
367 identification of Tau-positive animals using the cutoff signal intensity and then comparing against histological

368 confirmation of Tau pathology as a gold standard. A fitted curve was then generated against the empirical points  
369 plotted on the graphs. Qualitative and quantitative analysis of MRI images was performed in OsiriX (version 5.8.5,  
370 64-bit, Pixmeo SARL, Geneva, Switzerland) and MATLAB (version 2015a, MathWorks, Natick, MA).

371 **Immunofluorescence –** After the final MRI scan, the mice were euthanized and perfused extensively with 0.9%  
372 saline followed by 4% paraformaldehyde for 15 mins. The brains were then immersion-fixed in 4% formaldehyde  
373 for 48h at 4°C, transferred to 30% sucrose for cryoprotection and embedded in OCT. Phenotypic confirmation for  
374 the presence of phosphorylated tau and vimentin was done on 25µm thick brain sections. Antigen retrieval in  
375 pH=8.5 citrate buffer was executed in a 1200W GE microwave for 15mins. After 15 minutes of cooling 25µL of  
376 1:50 dilution of primary p-tau antibody namely either AT8,AT100 or AT180 that recognize different p-tau species  
377 were incubated in a tray (RPI, Mt. Prospect, IL #248270) designed for microwave enhanced immunostaining  
378 procedures for 3min at power level 3. After a 2 min cooling, sections were washed with PBS and incubated for  
379 3min with a 1:100 dilution of appropriate secondary antibody. DAPI staining proceeded after 2 mins of cooling  
380 and a PBS washing. ProGold Antifade (Invitrogen, Carlsbad, CA, # P36030) was used to mount slides which  
381 were visualized on Olympus Fluoview LV100. Scanning of whole sections was also conducted using a Biotek  
382 Cytation 5 slide scanning microscope. List of Antibodies – AT8 (#MN1020), Vimentin SP20 (#MA516409) both  
383 Thermo Fisher Scientific, Waltham, MA, Vimentin D21H3 (Cell Signaling Technology, Beverly, MA, #5741T,),  
384 Cell-surface vimentin (Abnova, Taipei City, Taiwan, #H00007431-M08J).

385 **Target Identification -** The protein targets of Tau-1, Tau-3, Tau-4 and Tau-5 were identified by affinity-pull down  
386 using the selected aptamers as the capturing reagent followed by mass-spectroscopy. A scrambled DNA  
387 sequence, R2, was used as a control. The hyperphosphorylated SH-SY5Y cells, at 90-95% confluence were  
388 washed with cold PBS buffer and incubated with biotinylated selected aptamers with 25mmol/l each at 4°C in  
389 PBS, respectively. After 2 hours of gentle agitation, SH-SY5Y cells were cross-linked with 1% formaldehyde for  
390 10 minutes at room temperature. The formaldehyde cross-linking was quenched with glycine. Cells were scraped  
391 from the plate, washed and lysed with lysing buffer (Thermofisher Scientific, # 87787) and treated with protease  
392 inhibitor mixture. The lysates were freeze-thawed for 30 minutes on ice and cleared by centrifuging at 10,000 xg  
393 for 2 minutes at 4°C. To pull down the cross-linked proteins, equal amounts of cell lysate were incubated with  
394 prewashed streptavidin magnetic beads for 1 hour at room temperature with continuous rotation. Protein  
395 digestions were performed on the beads to isolate targeted proteins and processed for mass spectrometric  
396 analysis. Each sample was analyzed in triplicates. The raw data files were processed to generate a Mascot

397 Generic Format with Mascot Distiller and searched against the SwissProt\_2012\_01 (Human) database using the  
398 licensed Mascot search engine v2.3.02 (Matrix Science, Boston, MA) run on an in-house server.

399 **References**

- 400 1. Goedert, M., Wischik, C. M., Crowther, R. A., Walker, J. E. & Klug, A. Cloning and sequencing of the  
401 cDNA encoding a core protein of the paired helical filament of Alzheimer disease: identification as the  
402 microtubule-associated protein tau. *Proc. Natl. Acad. Sci. U. S. A.* **85**, 4051–4055 (1988).
- 403 2. Goedert, M., Spillantini, M. G., Jakes, R., Rutherford, D. & Crowther, R. A. Multiple isoforms of human  
404 microtubule-associated protein tau: sequences and localization in neurofibrillary tangles of Alzheimer's  
405 disease. *Neuron* **3**, 519–526 (1989).
- 406 3. Iqbal, K., Liu, F. & Gong, C. Tau and neurodegenerative disease: the story so far. *Nat. Rev. Neurol.* **12**,  
407 15–27 (2016).
- 408 4. Guo, T., Noble, W. & Hanger, D. Roles of tau protein in health and disease. *Acta Neuropathol.* **133**,  
409 665–704 (2017).
- 410 5. Wang, Y. & Mandelkow, E. Tau in physiology and pathology. *Nat. Rev. Neurosci.* **17**, 22 (2016).
- 411 6. Chong, F. P., Ng, K. Y., Koh, R. Y. & Chye, S. M. Tau Proteins and Tauopathies in Alzheimer's  
412 Disease. *Cell. Mol. Neurobiol.* **38**, 965–980 (2018).
- 413 7. Karikari, T. K. *et al.* Distinct conformations, aggregation and cellular internalization of different tau  
414 strains. *Front. Cell. Neurosci.* **13**, 1–16 (2019).
- 415 8. d'Errico, P. & Meyer-Luehmann, M. Mechanisms of Pathogenic Tau and A $\beta$  Protein Spreading in  
416 Alzheimer's Disease. *Front. Aging Neurosci.* **12**, 1–10 (2020).
- 417 9. Brunello, C. A., Merezhko, M., Uronen, R. L. & Huttunen, H. J. Mechanisms of secretion and spreading  
418 of pathological tau protein. *Cell. Mol. Life Sci.* **77**, 1721–1744 (2020).
- 419 10. Vogel, J. W. *et al.* Spread of pathological tau proteins through communicating neurons in human  
420 Alzheimer's disease. *Nat. Commun.* **11**, 2612 (2020).
- 421 11. Gibbons, G. S., Lee, V. M. Y. & Trojanowski, J. Q. Mechanisms of Cell-to-Cell Transmission of

- 422 Pathological Tau: A Review. *JAMA Neurol.* **76**, 101–108 (2019).
- 423 12. Jack Jr, C. R. et al. NIA-AA research framework: toward a biological definition of Alzheimer's disease.  
424 *Alzheimer's Dement.* **14**, 535–562 (2018).
- 425 13. Jack, C. R. et al. A/T/N: an unbiased descriptive classification scheme for Alzheimer disease  
426 biomarkers. *Neurology* **87**, 539–547 (2016).
- 427 14. Selkoe, D. J. & Hardy, J. The amyloid hypothesis of Alzheimer's disease at 25 years. *EMBO Mol. Med.*  
428 **8**, 595–608 (2016).
- 429 15. Mattsson-Carlgren, N. et al. A $\beta$  deposition is associated with increases in soluble and phosphorylated  
430 tau that precede a positive Tau PET in Alzheimer's disease. *Sci. Adv.* **6**, (2020).
- 431 16. Leuzy, A. et al. Longitudinal tau and metabolic PET imaging in relation to novel CSF tau measures in  
432 Alzheimer's disease. *Eur. J. Nucl. Med. Mol. Imaging* **46**, 1152–1163 (2019).
- 433 17. Cummings, J. L. Biomarkers in Alzheimer's disease drug development. *Alzheimer's Dement.* **7**, e13–  
434 e44 (2011).
- 435 18. Smoler, M., Coceano, G., Testa, I., Bruno, L. & Levi, V. Apparent stiffness of vimentin intermediate  
436 filaments in living cells and its relation with other cytoskeletal polymers. *Biochim. Biophys. Acta - Mol.*  
437 *Cell Res.* **1867**, 118726 (2020).
- 438 19. Peskind, E., Nordberg, A., Darreh-Shori, T. & Soininen, H. Safety of lumbar puncture procedures in  
439 patients with Alzheimer's disease. *Curr. Alzheimer Res.* **6**, 290–292 (2009).
- 440 20. Wittenberg, R., Knapp, M., Karagiannidou, M., Dickson, J. & Schott, J. M. Economic impacts of  
441 introducing diagnostics for mild cognitive impairment Alzheimer's disease patients. *Alzheimer's  
442 Dement. Transl. Res. Clin. Interv.* **5**, 382–387 (2019).
- 443 21. Ehman, E. C. et al. PET/MRI: where might it replace PET/CT? *J. Magn. Reson. Imaging* **46**, 1247–1262  
444 (2017).
- 445 22. Leuzy, A. et al. Tau PET imaging in neurodegenerative tauopathies—still a challenge. *Mol. Psychiatry*  
446 **24**, 1112–1134 (2019).

- 447 23. Jack Jr, C. R. *et al.* Tracking pathophysiological processes in Alzheimer's disease: an updated  
448 hypothetical model of dynamic biomarkers. *Lancet Neurol.* **12**, 207–216 (2013).
- 449 24. Terry, R. D. *et al.* Physical basis of cognitive alterations in Alzheimer's disease: synapse loss is the  
450 major correlate of cognitive impairment. *Ann. Neurol. Off. J. Am. Neurol. Assoc. Child Neurol. Soc.* **30**,  
451 572–580 (1991).
- 452 25. Hyman, B. T. *et al.* National Institute on Aging–Alzheimer's Association guidelines for the  
453 neuropathologic assessment of Alzheimer's disease. *Alzheimer's Dement.* **8**, 1–13 (2012).
- 454 26. Montine, T. J. *et al.* National Institute on Aging–Alzheimer's Association guidelines for the  
455 neuropathologic assessment of Alzheimer's disease: a practical approach. *Acta Neuropathol.* **123**, 1–11  
456 (2012).
- 457 27. Wang, J.-Z., Xia, Y.-Y., Grundke-Iqbali, I. & Iqbal, K. Abnormal hyperphosphorylation of tau: sites,  
458 regulation, and molecular mechanism of neurofibrillary degeneration. *J. Alzheimer's Dis.* **33**, S123–  
459 S139 (2013).
- 460 28. Grundke-Iqbali, I. *et al.* Abnormal phosphorylation of the microtubule-associated protein tau (tau) in  
461 Alzheimer cytoskeletal pathology. *Proc. Natl. Acad. Sci.* **83**, 4913–4917 (1986).
- 462 29. Delobel, P. *et al.* Analysis of tau phosphorylation and truncation in a mouse model of human tauopathy.  
463 *Am. J. Pathol.* **172**, 123–131 (2008).
- 464 30. Lund, E. T., McKenna, R., Evans, D. B., Sharma, S. K. & Mathews, W. R. Characterization of the in  
465 vitro phosphorylation of human tau by tau protein kinase II (cdk5/p20) using mass spectrometry. *J.*  
466 *Neurochem.* **76**, 1221–1232 (2001).
- 467 31. Liu, F., Grundke-Iqbali, I., Iqbal, K. & Gong, C. Contributions of protein phosphatases PP1, PP2A, PP2B  
468 and PP5 to the regulation of tau phosphorylation. *Eur. J. Neurosci.* **22**, 1942–1950 (2005).
- 469 32. Mu, Q. *et al.* Conjugate-SELEX: A High-throughput Screening of Thioaptamer-liposomal Nanoparticle  
470 Conjugates for Targeted Intracellular Delivery of Anticancer Drugs. *Mol. Ther. - Nucleic Acids* **5**, e382  
471 (2016).
- 472 33. Parekh, P., Tang, Z., Turner, P. C., Moyer, R. W. & Tan, W. Aptamers Recognizing Glycosylated

- 473        Hemagglutinin Expressed on the Surface of Vaccinia Virus-Infected Cells. *Anal. Chem.* **82**, 8642–8649  
474        (2010).
- 475    34. Ayyagari, A. L. *et al.* Long-circulating liposomal contrast agents for magnetic resonance imaging. *Magn.*  
476        *Reson. Med. An Off. J. Int. Soc. Magn. Reson. Med.* **55**, 1023–1029 (2006).
- 477    35. Kamat, P. K., Rai, S., Swarnkar, S., Shukla, R. & Nath, C. Molecular and Cellular Mechanism of  
478        Okadaic Acid (OKA)-Induced Neurotoxicity: A Novel Tool for Alzheimer's Disease Therapeutic  
479        Application. *Mol. Neurobiol.* **50**, 852–865 (2014).
- 480    36. Gulaj, E., Pawlak, K., Bien, B. & Pawlak, D. Kynurenone and its metabolites in Alzheimer's disease  
481        patients. *Adv. Med. Sci.* **55**, 204–211 (2010).
- 482    37. The UniProt Consortium. UniProt: the universal protein knowledgebase in 2021. *Nucleic Acids Res.* **49**,  
483        D480–D489 (2021).
- 484    38. Rothberg, J. M. *et al.* An integrated semiconductor device enabling non-optical genome sequencing.  
485        *Nature* **475**, 348–352 (2011).
- 486    39. Lu, E., Elizondo-Riojas, M.-A., Chang, J. T. & Volk, D. E. Aptaligner: automated software for aligning  
487        pseudorandom DNA X-aptamers from next-generation sequencing data. *Biochemistry* **53**, 3523–3525  
488        (2014).
- 489    40. Katoh, K., Rozewicki, J. & Yamada, K. D. MAFFT online service: multiple sequence alignment,  
490        interactive sequence choice and visualization. *Brief. Bioinform.* **20**, 1160–1166 (2019).
- 491    41. Sievers, F. *et al.* Fast, scalable generation of high-quality protein multiple sequence alignments using  
492        Clustal Omega. *Mol. Syst. Biol.* **7**, 539 (2011).
- 493    42. Zuker, M. Mfold web server for nucleic acid folding and hybridization prediction. *Nucleic Acids Res.* **31**,  
494        3406–3415 (2003).
- 495    43. Donato, R. *et al.* Differential development of neuronal physiological responsiveness in two human  
496        neural stem cell lines. *BMC Neurosci.* **8**, 1–11 (2007).
- 497    44. Ghaghada, K., Hawley, C., Kawaji, K., Annapragada, A. & Mukundan Jr, S. T1 relaxivity of core-  
498        encapsulated gadolinium liposomal contrast agents—effect of liposome size and internal gadolinium

- 499 concentration. *Acad. Radiol.* **15**, 1259–1263 (2008).
- 500 45. Ghaghada, K. B. *et al.* New Dual Mode Gadolinium Nanoparticle Contrast Agent for Magnetic  
501 Resonance Imaging. *PLoS One* **4**, e7628 (2009).
- 502 46. Badachhape, A. A. *et al.* Pre-clinical dose-ranging efficacy, pharmacokinetics, tissue biodistribution,  
503 and toxicity of a targeted contrast agent for MRI of amyloid deposition in Alzheimer's disease. *Sci. Rep.*  
504 **10**, 16185 (2020).
- 505 47. Mattsson, N., Lönneborg, A., Boccardi, M., Blennow, K. & Hansson, O. Clinical validity of cerebrospinal  
506 fluid A $\beta$ 42, tau, and phospho-tau as biomarkers for Alzheimer's disease in the context of a structured 5-  
507 phase development framework. *Neurobiol. Aging* **52**, 196–213 (2017).
- 508 48. Coch, R. A. & Leube, R. E. Intermediate filaments and polarization in the intestinal epithelium. *Cells* **5**,  
509 32 (2016).
- 510 49. Cuingnet, R. *et al.* Automatic classification of patients with Alzheimer's disease from structural MRI: a  
511 comparison of ten methods using the ADNI database. *Neuroimage* **56**, 766–781 (2011).
- 512 50. Johansson, M. *et al.* Mild behavioral impairment and its relation to tau pathology in preclinical  
513 Alzheimer's disease. *Transl. Psychiatry* **11**, 1–8 (2021).
- 514 51. Suárez-Calvet, M. *et al.* Novel tau biomarkers phosphorylated at T181, T217 or T231 rise in the initial  
515 stages of the preclinical Alzheimer's continuum when only subtle changes in A $\beta$  pathology are detected.  
516 *EMBO Mol. Med.* **12**, e12921 (2020).
- 517 52. Mattsson, N. *et al.* 18 F-AV-1451 and CSF T-tau and P-tau as biomarkers in Alzheimer's disease .  
518 *EMBO Mol. Med.* **9**, 1212–1223 (2017).
- 519 53. Chung, S.-H. Aberrant phosphorylation in the pathogenesis of Alzheimer's disease. *BMB Rep.* **42**, 467–  
520 474 (2009).
- 521 54. Oliveira, J., Costa, M., de Almeida, M. S. C., da Cruz e Silva, O. A. B. & Henriques, A. G. Protein  
522 phosphorylation is a key mechanism in Alzheimer's disease. *J. Alzheimer's Dis.* **58**, 953–978 (2017).
- 523 55. Augustinack, J. C., Schneider, A., Mandelkow, E.-M. & Hyman, B. T. Specific tau phosphorylation sites  
524 correlate with severity of neuronal cytopathology in Alzheimer's disease. *Acta Neuropathol.* **103**, 26–35

- 525 (2002).
- 526 56. Wang, Y. & Mandelkow, E. Tau in physiology and pathology. *Nat. Rev. Neurosci.* **17**, 22–35 (2016).
- 527 57. Wang, J., Grundke-Iqbali, I. & Iqbali, K. Kinases and phosphatases and tau sites involved in Alzheimer
- 528 neurofibrillary degeneration. *Eur. J. Neurosci.* **25**, 59–68 (2007).
- 529 58. Sontag, J.-M. & Sontag, E. Protein phosphatase 2A dysfunction in Alzheimer's disease. *Front. Mol.*
- 530 *Neurosci.* **7**, 16 (2014).
- 531 59. Sontag, J. M., Nunbhakdi-Craig, V., White, C. L., Halpain, S. & Sontag, E. The protein phosphatase
- 532 PP2A/B $\alpha$  binds to the microtubule-associated proteins Tau and MAP2 at a motif also recognized by the
- 533 kinase Fyn: Implications for tauopathies. *J. Biol. Chem.* **287**, 14984–14993 (2012).
- 534 60. Franzmeier, N. *et al.* Functional brain architecture is associated with the rate of tau accumulation in
- 535 Alzheimer's disease. *Nat. Commun.* **11**, 1–17 (2020).
- 536 61. DeVos, S. L. *et al.* Synaptic tau seeding precedes tau pathology in human Alzheimer's disease brain.
- 537 *Front. Neurosci.* **12**, 267 (2018).
- 538 62. Dustin, D., Hall, B. M., Annapragada, A. & Pautler, R. G. Neuroimaging in Alzheimer's disease:
- 539 preclinical challenges toward clinical efficacy. *Transl. Res.* **175**, 37–53 (2016).
- 540 63. Takeuchi, H. *et al.* P301S mutant human tau transgenic mice manifest early symptoms of human
- 541 tauopathies with dementia and altered sensorimotor gating. *PLoS One* **6**, e21050 (2011).
- 542 64. Yoshiyama, Y. *et al.* Synapse loss and microglial activation precede tangles in a P301S tauopathy
- 543 mouse model. *Neuron* **53**, 337–351 (2007).
- 544 65. Holmes, B. B. *et al.* Proteopathic tau seeding predicts tauopathy in vivo. *Proc. Natl. Acad. Sci.* **111**,
- 545 E4376 LP-E4385 (2014).
- 546 66. Eriksson, J. E. *et al.* Introducing intermediate filaments: from discovery to disease. *J. Clin. Invest.* **119**,
- 547 1763–1771 (2009).
- 548 67. Sihag, R. K., Inagaki, M., Yamaguchi, T., Shea, T. B. & Pant, H. C. Role of phosphorylation on the
- 549 structural dynamics and function of types III and IV intermediate filaments. *Exp. Cell Res.* **313**, 2098–

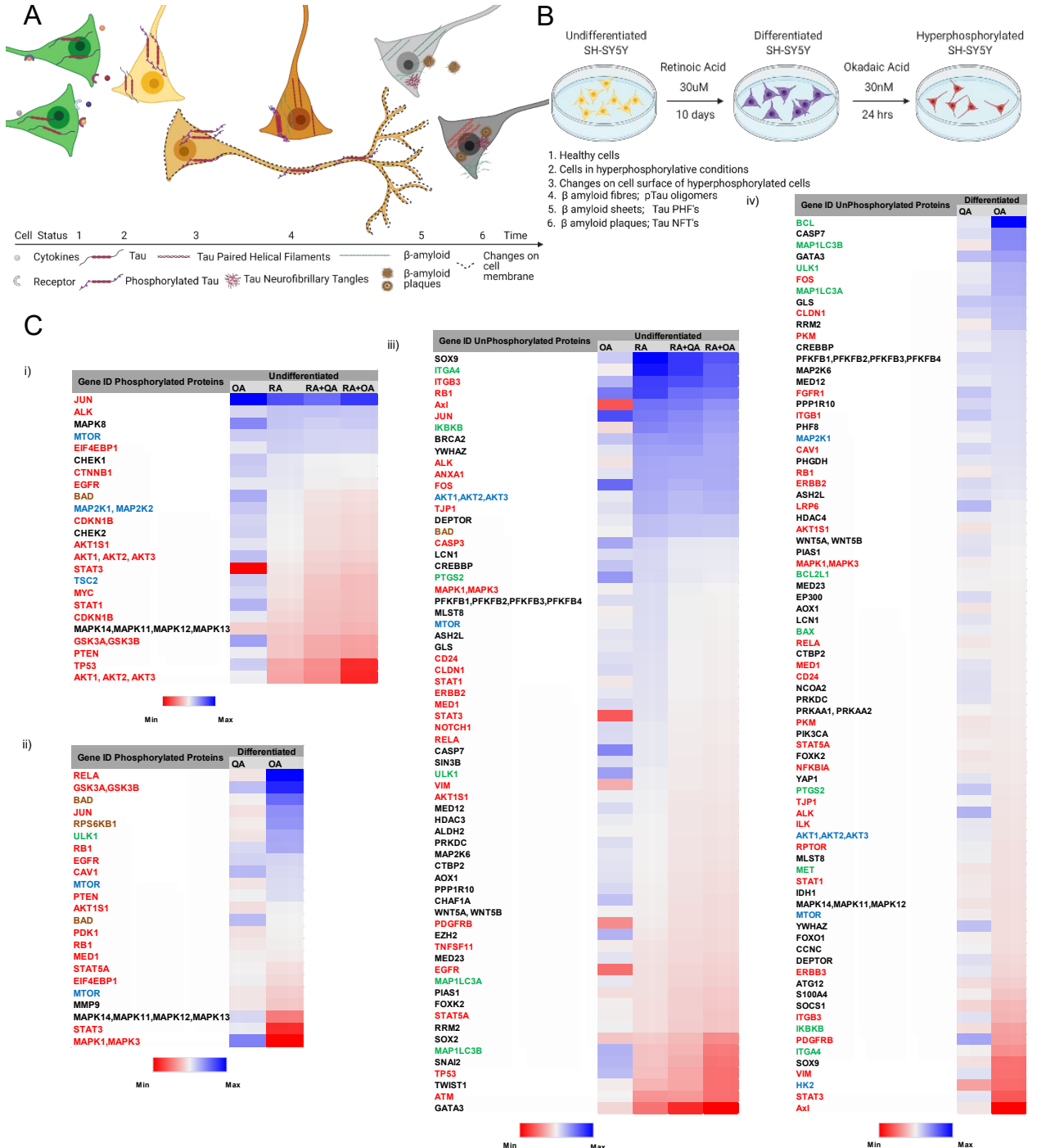
- 550                  2109 (2007).
- 551    68. Snider, N. T. & Omary, M. B. Post-translational modifications of intermediate filament proteins:  
552                  mechanisms and functions. *Nat. Rev. Mol. Cell Biol.* **15**, 163–177 (2014).
- 553    69. Battaglia, R. A., Delic, S., Herrmann, H. & Snider, N. T. Vimentin on the move: New developments in  
554                  cell migration [version 1; referees: 2 approved]. *F1000Research* **7**, 1–10 (2018).
- 555    70. Pattabiraman, S. *et al.* Vimentin protects differentiating stem cells from stress. *Sci. Rep.* **10**, 1–15  
556                  (2020).
- 557    71. Etienne-Manneville, S. Cytoplasmic Intermediate Filaments in Cell Biology. *Annu. Rev. Cell Dev. Biol.*  
558                  **34**, 1–28 (2018).
- 559    72. Ivaska, J., Pallari, H.-M., Nevo, J. & Eriksson, J. E. Novel functions of vimentin in cell adhesion,  
560                  migration, and signaling. *Exp. Cell Res.* **313**, 2050–2062 (2007).
- 561    73. Jones, J. C. R. *et al.* Intermediate filaments and the plasma membrane. *Cold Spring Harb. Perspect.  
562                  Biol.* **9**, (2017).
- 563    74. Kalluri, R. EMT: when epithelial cells decide to become mesenchymal-like cells. *J. Clin. Invest.* **119**,  
564                  1417–1419 (2009).
- 565    75. Ivaska, J. Vimentin: Central hub in EMT induction? *Small GTPases* **2**, 1436–1448 (2011).
- 566    76. Hameed, S. *et al.* Role of Fluid Biomarkers and PET Imaging in Early Diagnosis and its Clinical  
567                  Implication in the Management of Alzheimer's Disease. *J. Alzheimer's Dis. Reports* **4**, 21–37 (2020).
- 568    77. Lemoine, L. *et al.* Comparative binding properties of the tau PET tracers THK5117, THK5351, PBB3,  
569                  and T807 in postmortem Alzheimer brains. *Alzheimers. Res. Ther.* **9**, 1–13 (2017).
- 570    78. Baker, S. L., Harrison, T. M., Maass, A., La Joie, R. & Jagust, W. J. Effect of off-target binding on 18F-  
571                  Flortaucipir variability in healthy controls across the life span. *J. Nucl. Med.* **60**, 1444–1451 (2019).
- 572    79. Volk, D. E. & Lokesh, G. L. R. Development of phosphorothioate DNA and DNA thioaptamers.  
573                  *Biomedicines* **5**, 41 (2017).
- 574    80. Mu, Q. *et al.* Conjugate-SELEX: A high-throughput screening of thioaptamer-liposomal nanoparticle

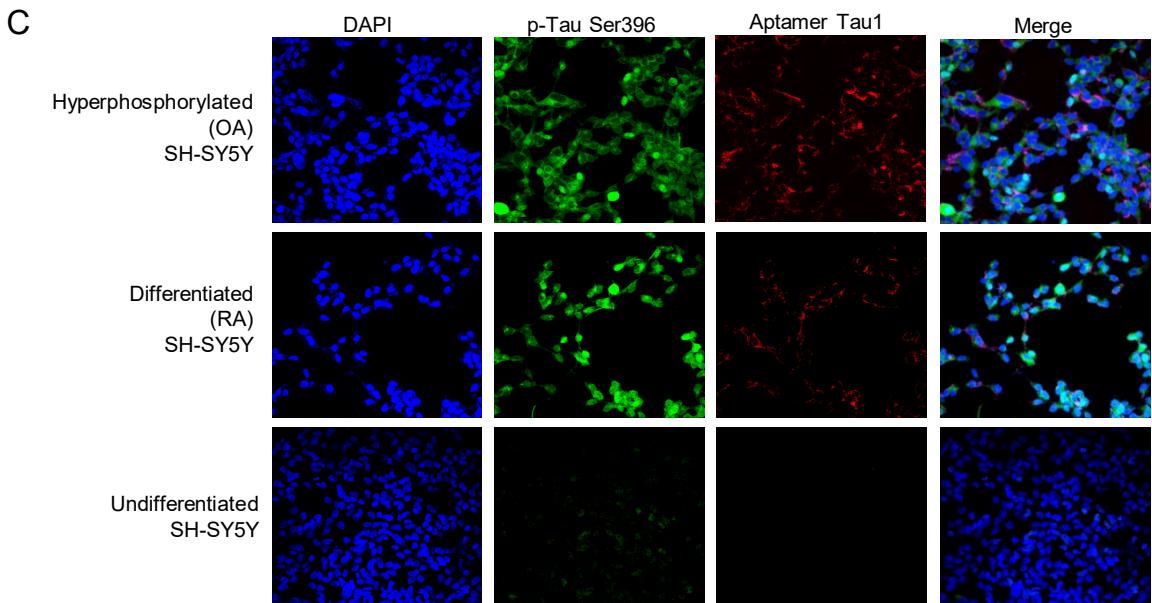
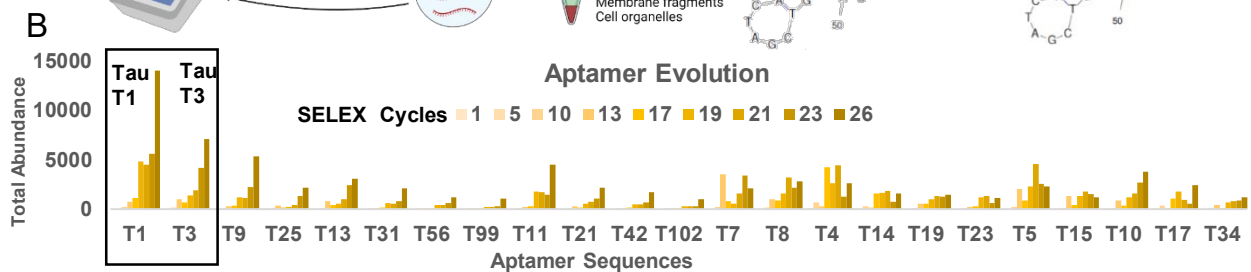
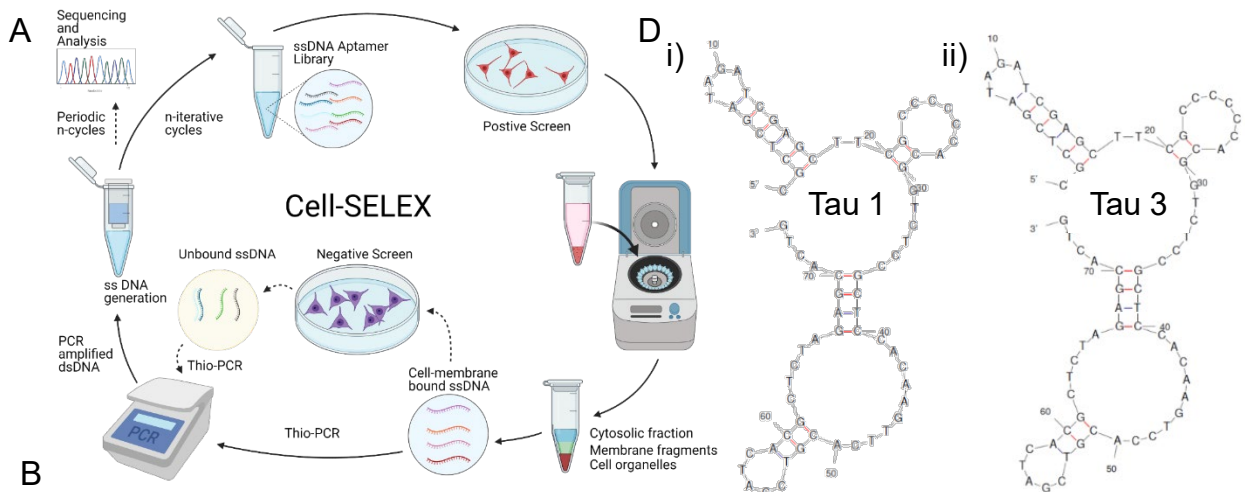
575 conjugates for targeted intracellular delivery of anticancer drugs. *Mol. Ther. Acids* **5**, e382 (2016).

576 **Acknowledgments:** We acknowledge the work of Dr. Igor Stupin (now deceased) in the handling, treatment,

577 and necropsy of all animals. **Funding:** This work was supported by Alzecca Biosciences, Inc. grants SRA 1, 2

578 and 3 to A.A.





**E**

Aptamer	Coverage %	Identity %	Sequence
1 Tau 1	100.0%	100.0%	-----CCCCCCCCTCG-----
2 Tau 3	100.0%	96.7%	-----CCCCCCCCTCG-----
3 Tau 9	100.0%	96.7%	-----CCCCCCCCTCG-----
4 Tau 25	100.0%	93.3%	-----CCCCCCCCTCG-----
5 Tau 13	100.0%	93.3%	-----CCCCCCCCTCG-----
6 Tau 31	100.0%	96.7%	-----CCCCCCCCTCG-----
7 Tau 56	100.0%	96.7%	-----CCCCCCCCTCG-----
8 Tau 99	100.0%	96.7%	-----CCCCCCCCTCG-----
9 Tau 11	96.7%	96.7%	-----CCCCCCCCTCG-----
10 Tau 21	96.7%	93.3%	-----CCCCCCCCTCG-----
11 Tau 42	96.7%	93.3%	-----CCCCCCCCTCG-----
12 Tau 102	96.7%	93.3%	-----CCCCCCCCTCG-----
13 Tau 7	96.7%	66.7%	-----CCCCCCCCTCG-----
14 Tau 8	83.3%	46.7%	-----CTCGTCCCAACATAC-----
15 Tau 4	83.3%	43.3%	-----CTCGTCCCAACATAC-----
16 Tau 14	83.3%	43.3%	-----CTCGTCCCAACATAC-----
17 Tau 19	83.3%	43.3%	-----CTCGTCCCAACATAC-----
18 Tau 23	83.3%	46.7%	-----CTCGTCCCAACATAC-----
19 Tau 5	90.0%	53.1%	-----CTCGTCCCAACATAC-----
20 Tau 15	90.0%	53.1%	-----CTCGTCCCAACATAC-----
21 Tau 10	73.3%	19.4%	-----CTCGTGGGTGTTGG-----
22 Tau 17	73.3%	22.6%	-----CTCGTGGGTGTTGG-----
23 Tau 34	86.7%	25.8%	-----TGGGTGTTGG-----

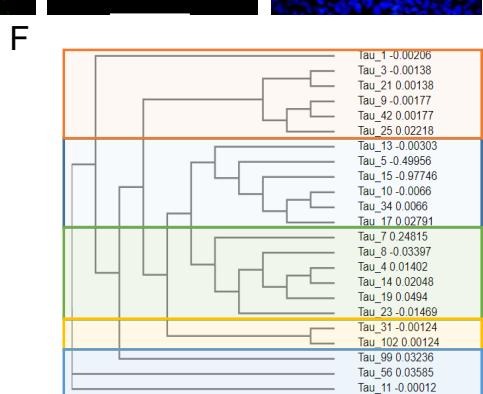


**Figure 2: Cell-SELEX to identify biomarkers onset of AD.** Okadaic acid treated differentiated SH-SY5Y cells were used as a surrogate for hyperphosphorylative neurons to screen DNA aptamers that specifically recognize the differences between the surfaces of treated and untreated cells, using the cell-SELEX methodology modified to capture membrane binding aptamers. (A) Pictorial representation of the cell-SELEX process (B) Abundance of the top 23 sequences from SELEX cycle 1 - 26 depicting their evolution. Note that the fractions are low until about cycle 10, when they increase sharply. Note that the abundance of Tau 1, Tau 3 continually increase with increasing cycle number. (C) Undifferentiated, differentiated (RA) and hyperphosphorylated (OA) SH-SY5Y cells stained with 50nM Cy5 labelled Tau1 aptamer for 2h at 4°C. (D) i) Tau 1 and ii) Tau 3 secondary structure using Mfold. (E) Multiple sequence alignment of the top 23 aptamer sequences by MAFFT. Note the existence of five families. (F) Cladogram showing relationship between the Tau aptamer sequences and the aptamer families.

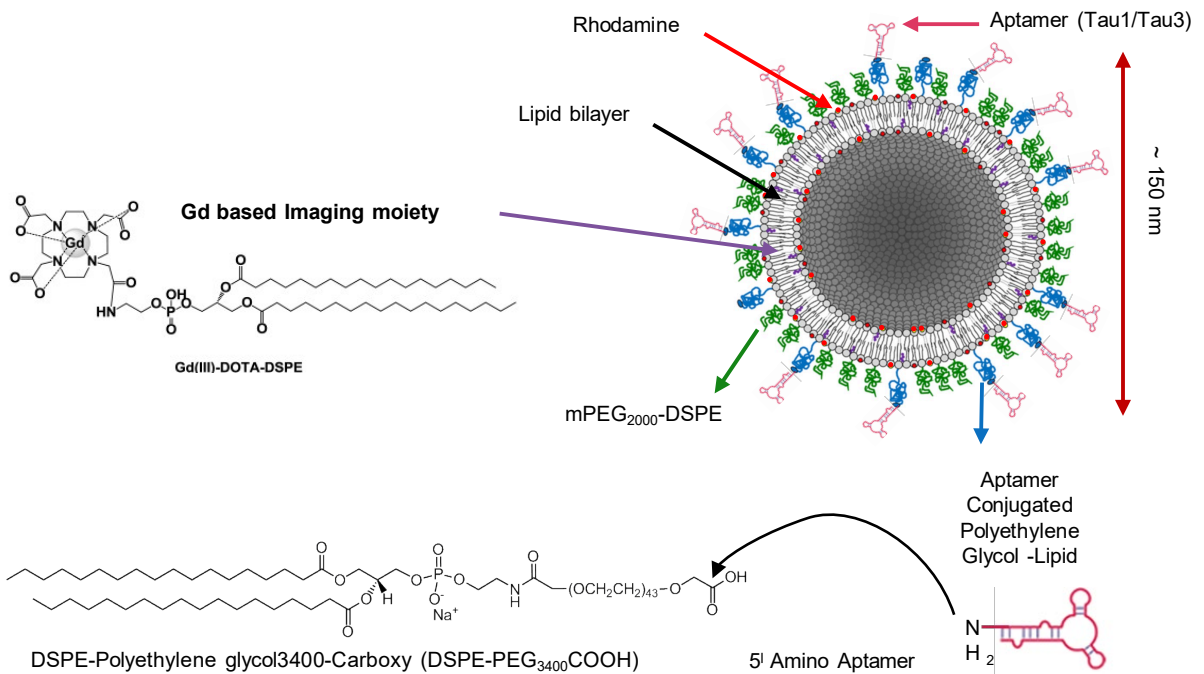


**Figure 3: Aptamer-targeted liposomal-Gd nanoparticle TauX contrast agent.** The liposomal bilayer incorporates DSPE-DOTA-Gd for MR contrast, DSPE-mPEG2000 to enhance circulation half-life, DSPE-PEG3400-aptamer (Tau1/Tau3) for targeting, and lissamine rhodamine for fluorescence imaging.

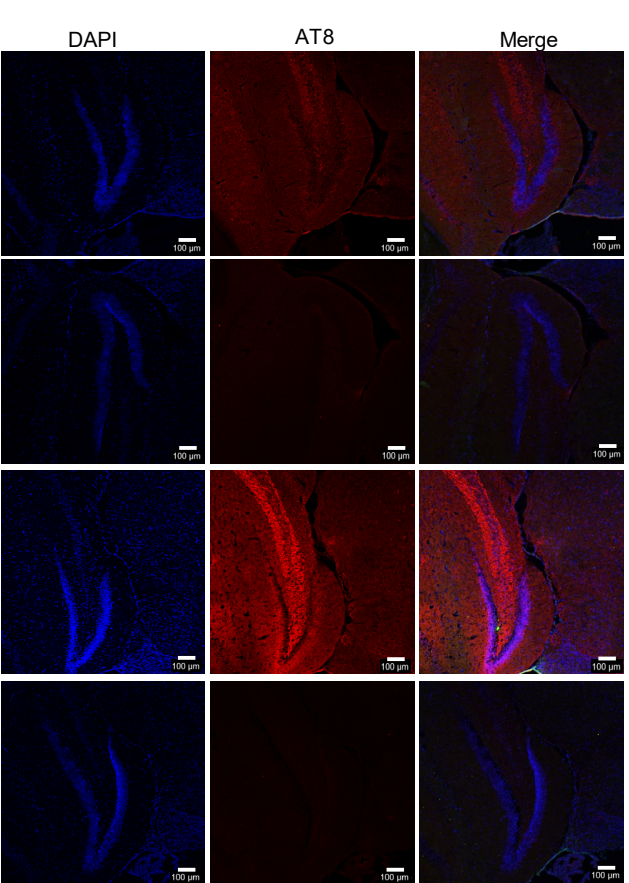
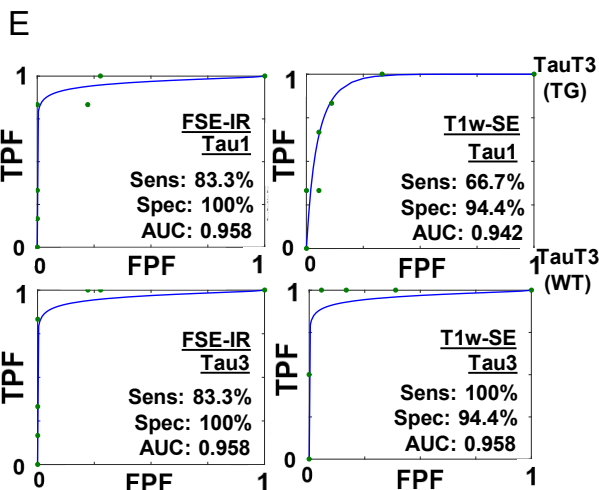
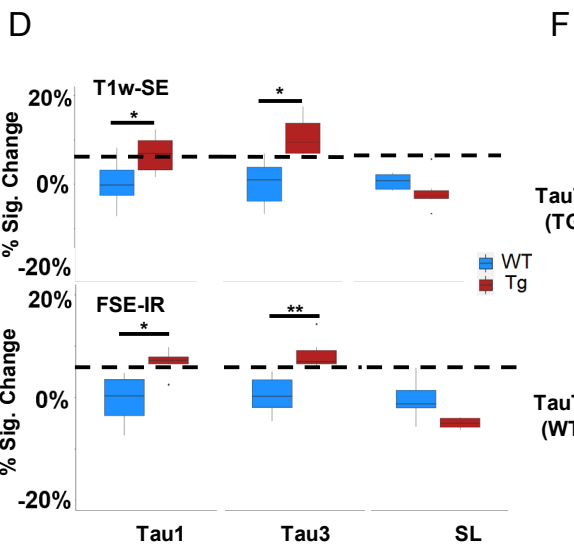
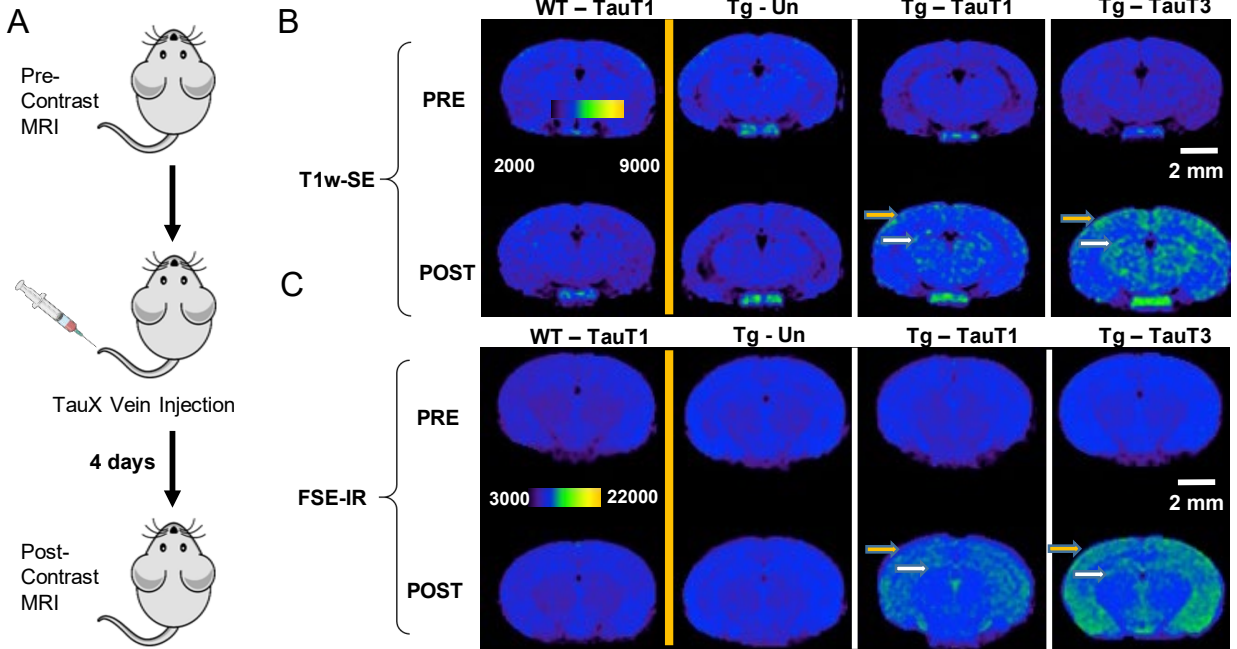


**Figure 4: Magnetic resonance imaging (MRI) and immunofluorescent staining demonstrate signal enhancement as TauX binds to hyperphosphorylated tau *in vivo*.** (A) Two month old mice were injected with 0.17 mmol Gd/kg dose TauX. Pre- and post-contrast images for (B)T1-weighted spin echo (T1w-SE) and (C) fast spin echo inversion recovery (FSE-IR) demonstrate signal enhancement in delayed post-contrast scans of transgenic (Tg) P301S mice treated with TauX relative to age-matched wild type (WT) controls. Tg animal showed high enhancement in cortical (yellow arrow) and hippocampal regions (white arrow). Transgenic animal shows no signal enhancement four days after injection of untargeted contrast (UC). Scale bar represents 2 mm. All animals are shown on the same color scale. (D) Box and whisker plots demonstrate signal enhancement in TG animals relative to WT counterparts and UC-treated Tg animals for both T1w-SE and FSE-IR sequences (\*p<0.05 ; \*\*p<0.005). Dotted line indicates signal threshold for determining sensitivity (2 standard deviations above baseline noise, ~6%). (E) Receiver operating characteristic (ROC) curves plotting true positive fraction (TPF) against false positive fraction (FPF) demonstrate TauX accuracy in identifying early age Tg animals. A fitted curve (blue) connects the observed operating points. Area under curve (AUC) is calculated using the fitted curve, and sensitivity (true positive rate) and specificity (true negative rate) for both formulations are listed. (F) The mice selected for TauX injection were genotyped which only revealed the presence of transgene. We confirmed the presence of hyperphosphorylated tau species in the mice by immunofluorescence on the brains sections harvested post MRI scans. Brains were perfused with heparin-PBS and fixed in OCT. IF with antibody AT8 probed for presence of ptau species provided high concordance with genotype confirming the presence of hyperphosphorylative conditions in the mice.

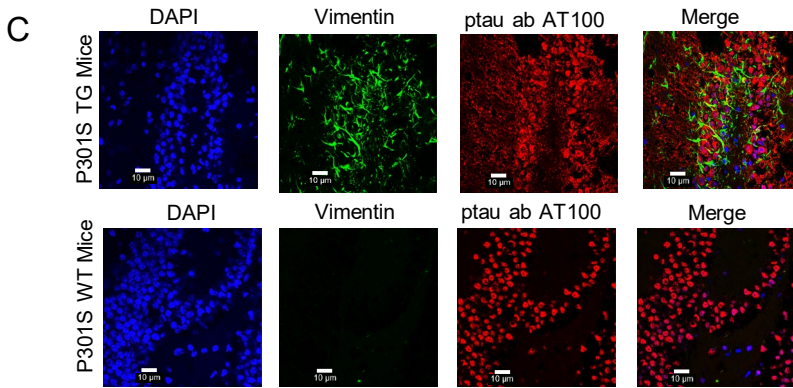
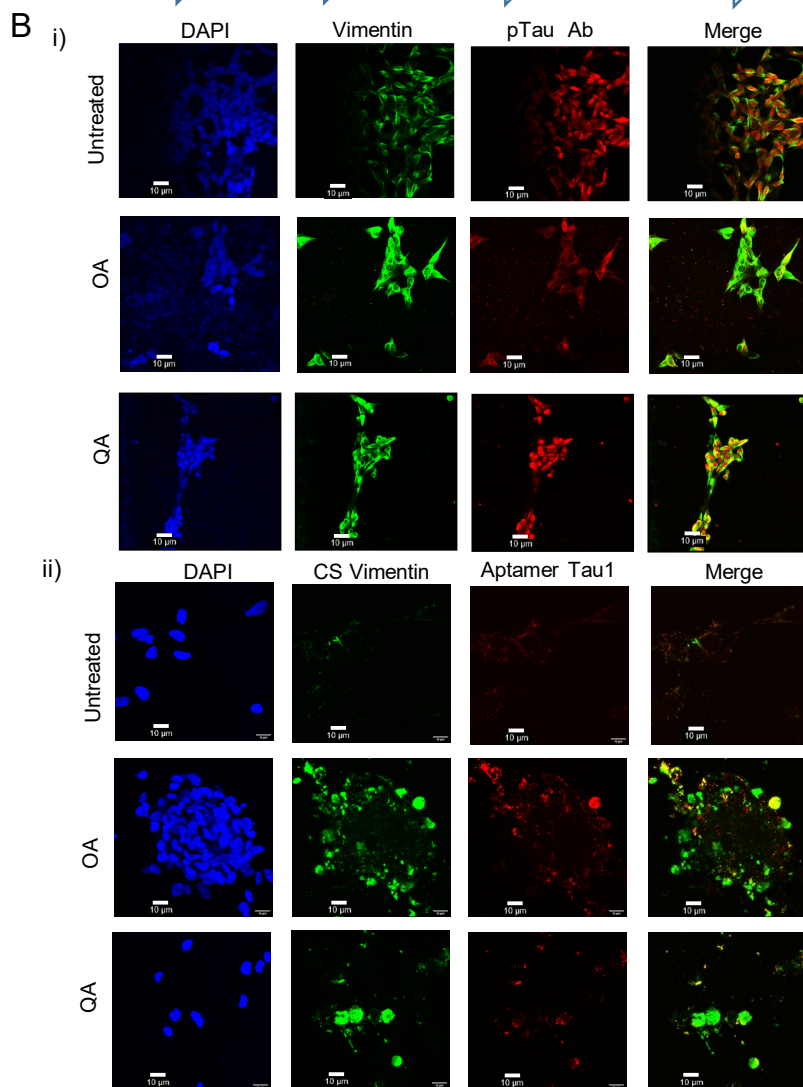
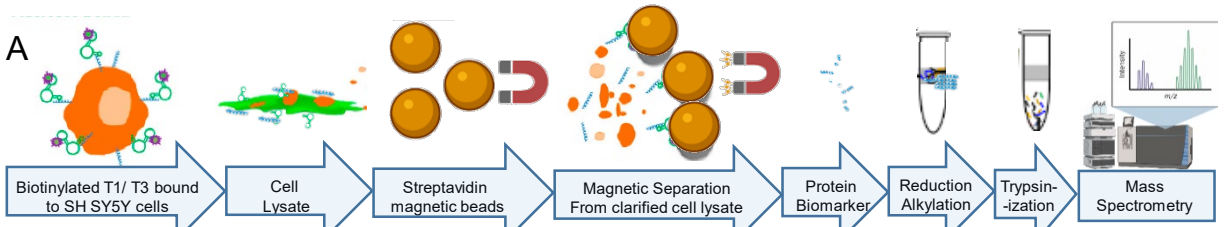
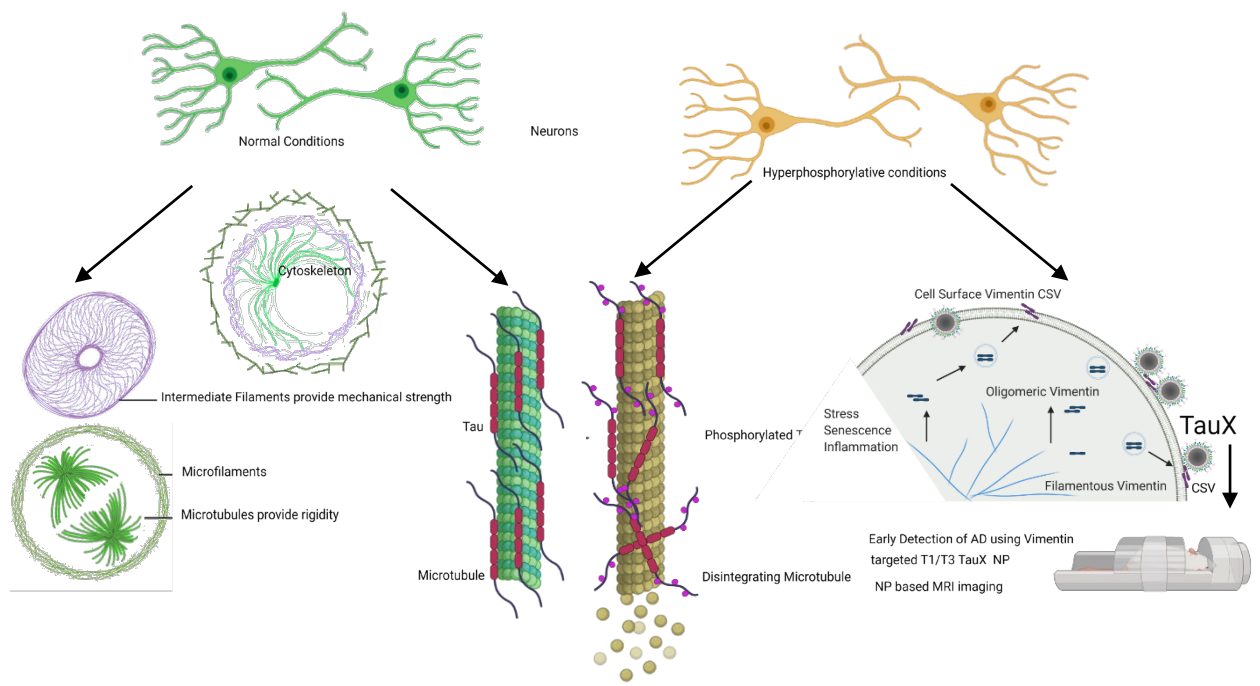


**Figure 5: Proteomic analysis for aptamer target identification.** A. Tryptic digest of aptamer bound cell membrane analyzed by LC/MS/MS. The raw data files were processed and searched against the SwissProt 2012 01 (Human) database. Vimentin was identified as possible target. B. Presence of the aptamers binding target on SH SY5Y cells; undifferentiated and hyperphosphorylated OA (24h, 30nM) and QA (24h, 100nM); i) co-stained with Vimentin (D21H3) and ptau (AT100) antibodies or ii) cell surface (CS) vimentin (Clone 84-1) antibody and aptamer T1 (50nM); nuclei counterstained with DAPI. C. Expression of Vimentin in P301S TG and WT frozen mouse tissue sections stained with Vimentin (SP20) and ptau (AT100) antibodies and DAPI stained nuclei.



**Graphical Abstract: Early detection of Tau pathology.** Hyperphosphorylative conditions provoke neuronal cells to undergo changes including on the cell surface. Translocation of Vimentin to the cell surface was exploited to generate an aptamer that was developed for *in vivo* use as targeted liposomal nanoparticle TauX for early MRI detection of tau pathology in a mouse model

**Supplementary Table 1: Target Identification using aptamer immunoprecipitation and mass spectrometry.** Aptamer based immunoprecipitation was performed. Mass-Spectrometric analysis of the trypsin digested aptamer-bound complex was analyzed by LC/MS/MS on an LTQ-Orbitrap-XLmass spectrometer with an Nanoflex system. The raw data files were processed and searched against the SwissProt\_2012\_01 (Human) database using the Mascot search engine. Exponentially modified protein abundance index (emPAI) are reported in the table below that report protein content proportional to protein content in a mixture.

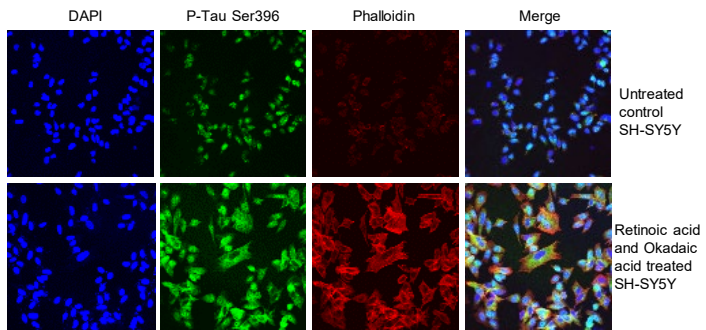
**T1 emPAI Target ID Aptamer Tau1**

6.3260 kDa heat shock protein, mitochondrial OS=Homo sapiens GN=HSPD1 PE=1 SV=2
3.49Keratin, type II cytoskeletal 1 OS=Homo sapiens GN=KRT1 PE=1 SV=6
1.29Keratin, type II cytoskeletal 2 epidermal OS=Homo sapiens GN=KRT2 PE=1 SV=2
0.38Keratin, type II cytoskeletal 6B OS=Homo sapiens GN=KRT6B PE=1 SV=5
0.38Keratin, type II cytoskeletal 6A OS=Homo sapiens GN=KRT6A PE=1 SV=3
0.11Keratin, type II cytoskeletal 5 OS=Homo sapiens GN=KRT5 PE=1 SV=3
4.67Keratin, type I cytoskeletal 10 OS=Homo sapiens GN=KRT10 PE=1 SV=6
1.66Keratin, type I cytoskeletal 9 OS=Homo sapiens GN=KRT9 PE=1 SV=3
0.97Keratin, type I cytoskeletal 14 OS=Homo sapiens GN=KRT14 PE=1 SV=4
0.69Keratin, type I cytoskeletal 17 OS=Homo sapiens GN=KRT17 PE=1 SV=2
5.01Single-stranded DNA-binding protein, mitochondrial OS=Homo sapiens GN=SSBP1 PE=1 SV=1
2.35Actin, cytoplasmic 1 OS=Homo sapiens GN=ACTB PE=1 SV=1
<b>0.13Vimentin OS=Homo sapiens GN=VIM PE=1 SV=4</b>
3.640S ribosomal protein S5 (Fragment) OS=Homo sapiens GN=RPS5 PE=1 SV=1
0.2Microtubule-associated protein 1B OS=Homo sapiens GN=MAP1B PE=1 SV=2
1.27Elongation factor 1-alpha 1 OS=Homo sapiens GN=EEF1A1 PE=1 SV=1
1.07Cofilin 1 (Non-muscle), isoform CRA_a OS=Homo sapiens GN=CFL1 PE=1 SV=1
0.28Leucine-rich PPR motif-containing protein, mitochondrial OS=Homo sapiens GN=LRPPRC PE=1 SV=3
2.74Peptidyl-prolyl cis-trans isomerase B OS=Homo sapiens GN=PPIB PE=1 SV=2
2.35Alpha-enolase OS=Homo sapiens GN=ENO1 PE=1 SV=2
0.61Stress-70 protein, mitochondrial OS=Homo sapiens GN=HSPA9 PE=1 SV=2
1.91ATP synthase subunit O, mitochondrial OS=Homo sapiens GN=ATP5O PE=1 SV=1
0.73Serpin H1 OS=Homo sapiens GN=SERPINH1 PE=1 SV=2
0.53ATP synthase subunit alpha, mitochondrial OS=Homo sapiens GN=ATP5A1 PE=1 SV=1
0.61ATP synthase subunit gamma, mitochondrial OS=Homo sapiens GN=ATP5C1 PE=1 SV=1
0.94Tubulin beta chain OS=Homo sapiens GN=TUBB PE=1 SV=1
0.97Nascent polypeptide-associated complex subunit alpha (Fragment) OS=Homo sapiens GN=NACA PE=1 SV=1
0.2578 kDa glucose-regulated protein OS=Homo sapiens GN=HSPA5 PE=1 SV=2

**T3 emPAI Target ID Aptamer Tau3**

4.45Keratin, type II cytoskeletal 1 OS=Homo sapiens GN=KRT1 PE=1 SV=6
2.92Keratin, type II cytoskeletal 2 epidermal OS=Homo sapiens GN=KRT2 PE=1 SV=2
<b>2.7Vimentin OS=Homo sapiens GN=VIM PE=1 SV=4</b>
0.43Keratin, type II cytoskeletal 5 OS=Homo sapiens GN=KRT5 PE=1 SV=3
5.32Keratin, type I cytoskeletal 10 OS=Homo sapiens GN=KRT10 PE=1 SV=6
0.45Keratin, type I cytoskeletal 14 OS=Homo sapiens GN=KRT14 PE=1 SV=4
1.81T-cell receptor alpha joining 56 (Fragment) OS=Homo sapiens GN=TRAJ56 PE=4 SV=1
2.62Actin, cytoplasmic 1 OS=Homo sapiens GN=ACTB PE=1 SV=1
2.35Actin, cytoplasmic 2 OS=Homo sapiens GN=ACTG1 PE=1 SV=1
0.46Actin, aortic smooth muscle OS=Homo sapiens GN=ACTA2 PE=1 SV=1
0.37Serum albumin OS=Homo sapiens GN=ALB PE=1 SV=1
1.16Keratin, type I cytoskeletal 9 OS=Homo sapiens GN=KRT9 PE=1 SV=3
0.6960 kDa heat shock protein, mitochondrial OS=Homo sapiens GN=HSPD1 PE=1 SV=2
0.12Myosin-9 OS=Homo sapiens GN=MYH9 PE=1 SV=4
0.1Isoform 2 of Myosin-10 OS=Homo sapiens GN=MYH10
0.72Nascent polypeptide-associated complex subunit alpha (Fragment) OS=Homo sapiens GN=NACA PE=1 SV=1
0.1Nestin OS=Homo sapiens GN=NES PE=1 SV=2
0.71Single-stranded DNA-binding protein, mitochondrial OS=Homo sapiens GN=SSBP1 PE=1 SV=1
0.2340S ribosomal protein S12 OS=Homo sapiens GN=RPS12 PE=1 SV=3
0.7Serpin H1 (Fragment) OS=Homo sapiens GN=SERPINH1 PE=1 SV=2
0.43Transcription factor BTF3 homolog 4 OS=Homo sapiens GN=BTF3L4 PE=1 SV=1
0.29Reticulocalbin-2 OS=Homo sapiens GN=RCN2 PE=1 SV=1
0.26Prelamin-A/C OS=Homo sapiens GN=LMNA PE=1 SV=1
0.12THO complex subunit 4 OS=Homo sapiens GN=ALYREF PE=1 SV=1
0.16Nuclease-sensitive element-binding protein 1 (Fragment) OS=Homo sapiens GN=YBX1 PE=1 SV=1
0.3Peptidyl-prolyl cis-trans isomerase B OS=Homo sapiens GN=PPIB PE=1 SV=2
0.1Isoform 2 of Heat shock protein HSP 90-alpha OS=Homo sapiens GN=HSP90AA1
0.12Heat shock protein HSP 90-beta OS=Homo sapiens GN=HSP90AB1 PE=1 SV=4

**Supplementary Figure 1: Hyperphosphorylative conditions.** SH SY5Y cells differentiated with 30 $\mu$ M Retinoic acid for 10days were exposed to 30nM Okadaic acid for 24hrs. Under these hyperphosphorylative conditions tau is overexpressed and hyperphosphorylated. Figure shows the presence of p-tau 396 in SH SY5Y cells in hyperphosphorylative conditions..



**Supplementary Figure 2: Apparent dissociation constants of Aptamer Tau1 and Tau3Target.** SH SY5Y and ReN cells were grown in 96-well plates, Retinoic acid was used for differentiation. Okadaic acid for SH SY5Y and quinolinic acid for ReN cells was used to generate hyperphosphorylative conditions. Saturation binding curves were generated using Cy5 labelled Tau1 and Tau3 using a microplate fluorescent reader. The binding constant  $K_d$  apparent was calculated using the inbuilt non-linear regression module using the equation  $Y = B_{max} \cdot X / (K_d + X)$  in Graph Pad Prism. \* error bars smaller than symbol not visualized

